Cement and Concrete Research 136 (2020) 106171

Contents lists available at ScienceDirect

Cement and Concrete Research

journal homepage: www.elsevier.com/locate/cemconres

Mechanical properties of struvite-K: A high-pressure X-ray diffraction study

Jiaqi Li*, Wenxin Zhang, Paulo J.M. Monteiro

Department of Civil and Environmental Engineering, University of California, Berkeley, CA 94720, United States

ARTICLE INFO

Keywords:
Magnesium potassium phosphate cement
High-pressure X-ray diffraction
Mechanical properties
Bulk modulus
Phase transition

ABSTRACT

Magnesium potassium phosphate cement (MKPC) is gaining increasing popularity for specialized applications, e.g., structural rehabilitation, waste encapsulation, and 3D printing. However, the mechanical properties of struvite-K, the binding phase of MKPC, have rarely been examined. This study utilized synchrotron-based high-pressure X-ray diffraction to determine the intrinsic mechanical properties of struvite-K at the unit-cell scale, for the first time. The deformation of the unit cell, axial incompressibility, and bulk modulus was studied under hydrostatic pressures up to ~10 GPa. The unit cell shifts from orthorhombic to monoclinic lattice below 1 GPa; phase transition and amorphization occur at ~5 and ~10 GPa, respectively. The axial incompressibility shifts from anisotropy to isotropy, and the bulk modulus increases from 27 to 37 GPa upon phase transition. The experimental results are of great importance in calibration of atomistic modelling and provide implications on the problem with nanoindentation for studying mechanical properties of struvite-K or MKPC.

1. Introduction

Magnesium potassium phosphate cement (MKPC), also termed chemically-bonded phosphate ceramics [1], has strong chemical bonding, low drying shrinkage, and high resistance to salts [2–4]. MKPC is often used in structural rehabilitation due to its strong bonding, high early strength, and rapid setting [5–7]. The relatively low pH and resistance to salts of MKPC favor its applications in the encapsulation of hazardous wastes (e.g., municipal solid waste and industrial wastes) and protection of aluminum and reactor vessels [3,8–12]. Applications of MKPC to bone and dental restorations have also been reported [13–15]. 3-dimensional (3D) printing of MKPC can be achieved due to rapid setting, and recent attempt at 3D printing of MKPC have indicated broader applications of MKPC-based materials [16,17]. Thus, MKPC has attracted significant interest in related research fields.

MKPC is a ternary system consisting of periclase (MgO), monopotassium phosphate (KH_2PO_4), and water. The acid-base reaction between MgO and KH_2PO_4 generates a large amount of heat, forming struvite-K ($MgKPO_4{\cdot}6H_2O$, as termed MKP in a few MKPC studies) as the primary final product [18], possibly with intermediate products (e.g., phosphorrösslerite ($MgKPO_4{\cdot}7H_2O$), newberyite ($MgKPO_4{\cdot}3H_2O$), and $Mg_2KH(PO_4)_2{\cdot}15H_2O$) during the first hours of reactions [19,20]. Cattiite ($MgKPO_4{\cdot}22H_2O$) often forms in a highly diluted MKPC system, e.g., at water-to-solid ratios > 100 [21]. Struvite-K is a rare mineral in the crust [22], but it also occurs as urinary calculi (urolith, e.g., kidney stone) in animal bodies [23,24]. The unit cell of struvite-K holds the space group of $Pmn2_1$ [22] (Fig. 1). The orthorhombic lattice parameters of natural and synthetic struvite-K at ambient pressure and temperature were reported as a = 6.87–6.90 Å, b = 6.16–6.17 Å, and c = 11.10–11.15 Å [22]. K—O pentahedra and Mg—O octahedra share either corner or edge, and they bond to P—O tetrahedra mainly through hydrogen bonds.

The mechanical properties of MKPC are undoubtedly important as they affect the performances and behavior of MKPC and MKPC-repaired materials. The strength of MKPC materials has been extensively studied in recent decades [25–27]. The influences of fly ash [28,29], wollastonite [30], magnesium-to-phosphate ratio [27,31,32], water-to-cement ratio [31,33,34], MgO reactivity [35,36], and fibers [37] on the strength developments of MKPC-based materials have been explored. The elastic modulus of hardened MKPC has been studied using mechanical loading and ultrasonic pulse at the macro scale [38,39]. Recent attempts at homogenization modelling of MKPC pastes indicated the potential of linking the microstructure and mechanical properties of MKPC-based materials [40,41]. The mechanical properties of struvite-K have rarely been explored [42,43]. The mechanical properties of struvite-K are important in homogenization modelling (Mori-Tanaka and self-consistent methods) and multiscale modelling of struvite-K based products and the MKPC-repaired materials (e.g., repaired concrete structures) and the optimization of MKPC products in service.

The elastic modulus of struvite-K was reported to be 22 GPa in a nanoindentation study [44,45]. In contrast, the elastic modulus of

* Corresponding author at: 115 Davis Hall, University of California, Berkeley, California 94720, United States.
E-mail address: Jiaqi.li@berkeley.edu (J. Li).

https://doi.org/10.1016/j.cemconres.2020.106171
Received 4 June 2020; Received in revised form 2 July 2020; Accepted 10 July 2020

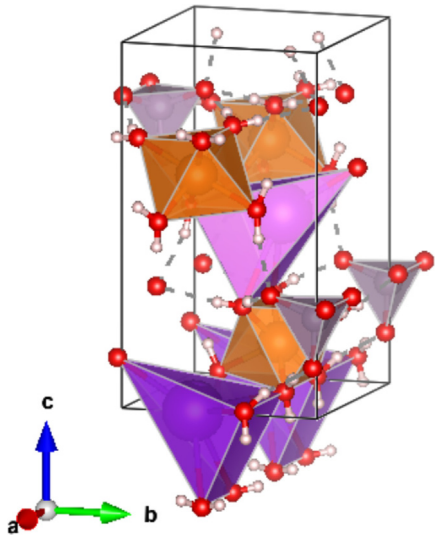

Fig. 1. Unit cell of struvite-K with K—O pentahedra in purple, Mg—O octahedra in orange, PO_4 in grey, O atom in red, H atom in white, and hydrogen bond as dash line [22]. (For interpretation of the references to colour in this figure legend, the reader is referred to the web version of this article.)

struvite-K was suggested to be 37.3 GPa in another nanoindentation study [40]. The experimental results from nanoindentation studies are strongly subject to characteristic depth, indent spacing, packing density, and pore structure of the sample [40,46] and preferred orientation of struvite-K crystals [22,47]. A molecular dynamics study of the mechanical properties of struvite-K avoided the above-mentioned experimental difficulties [43]. However, the gap between the structure and mechanical properties of struvite-K remains, as the simulated properties at the unit-cell scale have not been validated by experimental studies. Thus, a more reliable characterization technique is needed to untangle the challenges in determining the mechanical properties of struvite-K. Synchrotron radiation-based high-pressure X-ray diffraction (HP-XRD) can probe the deformation of materials at the unit-cell scale. HP-XRD has been recognized as a reliable technique to probe the mechanical properties of porous crystalline cement-based phases [48–50]. Here, for the first time, we experimentally determined the mechanical properties of struvite-K. The hydrostatic pressure-induced axial and volumetric changes of struvite-K crystal lattice were measured using HP-XRD and the results were used to calculate its bulk modulus. This work aims to understand the structure and mechanical behavior of struvite-K, which are essentially critical in optimizing the properties of MKPC using a bottom-up design from the lowest level of their hierarchical structure.

2. Methods

2.1. Sample preparation

Struvite-K was prepared by adding KOH solution dropwise to a solution of 10.68 g $MgC1_2{\cdot}6H_2O$ and 25 g KH_2PO_4 in 94.32 g deionized water until the pH reached 7.5 at room temperature [51]. At 100 days, the sample was vacuum filtered with a 0.45-μm nylon filter. The remaining solid was stored in a N_2-filled desiccator with a humidity trap prepared from saturated $CaCl_2$ solution (~30% relative humidity). The dry struvite-K sample was ground by hand before the first set of measurements. For a repetitive set of measurements, the dry sample was not ground. The purity of struvite-K formed from this precipitation method was confirmed using diffraction, see below.

2.2. High pressure X-ray diffraction (HP-XRD)

The HP-XRD experiment was performed at the beamline 12.2.2 of the Advanced Light Source at Lawrence Berkeley National Laboratory, using a synchrotron monochromatic x-ray and a Merrill-Bassett diamond anvil cell. A stainless-steel gasket was pre-indented to a thickness of ~110 um by the diamond anvil pair (culet diameter ~300 μm), then a cylindrical chamber with a diameter of ~110 μm was drilled at the center of the indent by laser milling. A small ruby sphere (0.05 wt% Cr^{3+} doped α-Al_2O_3) was loaded into the chamber after the loading of struvite-K powder. Subsequently, the chamber was filled with pressure-transmitting medium (methanol: ethanol = 4:1 by volume), then immediately sealed by the diamond anvil pair. The ruby fluorescence technique was used offline to determine the hydrostatic pressure. The wavelength of the incident beam was calibrated to 0.4959 Å, and the sample-to-detector distance was ~330 mm. The beam size was ~30 μm. Struvite-K at the ambient pressure was loaded into a glass capillary before analysis. Diffractions of struvite-K at elevated hydrostatic pressure were measured in the diamond anvil cell. Two repetitive measurements at elevated pressure were conducted. The raw data (2D image) were processed using Dioptas [52]. XFIT code [53] was used to deconvolute peaks or diffuse scattering of all data. Peak type was selected to be PVII (Split Pearson functions), and the fitting methods was Marquardt. Celref [54] was used for structural refinement at all pressures (peaks positions are the only inputs). The lattice parameters a, b, c, and γ are refined while α and β are fixed at 90°.

The pressure-dependent volumetric change is described by the third-order Birch-Murnaghan equation of state (BM-EoS) Eq. (1):

$$P(V) = \frac{3}{2}K_0\left[\left(\frac{V}{V_0}\right)^{-\frac{7}{3}} - \left(\frac{V}{V_0}\right)^{-\frac{5}{3}}\right]\left[1 + \frac{3}{4}(K_0' - 4)\left(\left(\frac{V}{V_0}\right)^{-\frac{2}{3}} - 1\right)\right] \quad (1)$$

where P is the pressure applied to a material, V_0 is the volume of unit cell at ambient pressure; V is the volume of unit cell; K_0 and K_0' are the bulk modulus and its derivative, respectively, at ambient pressure. K_0' is suggested to be fixed at 4 when the measured pressure range is too low or too high and only a small number of data points are taken [55,56] and Eq. (2) is reorganized into a simplified second-order form.

$$P = \frac{3}{2}K_0\left[\left(\frac{V}{V_0}\right)^{-\frac{7}{3}} - \left(\frac{V}{V_0}\right)^{-\frac{5}{3}}\right] \quad (2)$$

The volume of a unit cell, V, is calculated with the refined lattice parameters at each pressure as Eq. (3):

$$V = abc(1 - \cos^2\alpha - \cos^2\beta - \cos^2\gamma + 2\cos\alpha\cos\beta\cos\gamma)^{1/2} \quad (3)$$

where a, b, and c are the lengths of the unit cell edges, and α, β, and γ are the angles between the edges.

3. Results and discussion

Diffraction patter of the sample at ambient pressure is shown in the top of Fig. 2. Impurity of the sample is below the detection limit of XRD. The powder diffractograms of struvite-K under increasing and decreasing hydrostatic pressures are shown in Fig. 2. The diffractogram at ambient pressure shows the typical diffraction pattern of struvite-K with the absence of any magnesium phosphate (hydrate) secondary products. Pronounced shifts in peak positions with increased hydrostatic pressures were observed due to reduced interplanar distances caused by the compression of the struvite-K lattice structure from all directions. As the applied pressure increased up to 4.7 GPa, the absolute intensity of most peaks monotonously decreased, accompanied by evident peak broadening. As a few peaks merged into diffuse scatterings, we used XFIT code [53] to deconvolute peaks (e.g., (022) and (212)) from the diffuse scattering (see an example in Supplementary Information). The peak-broadening and decreased peak intensity are attributed to the increased stress-induced structural disordering at elevated pressures. These phenomena are commonly found in high-

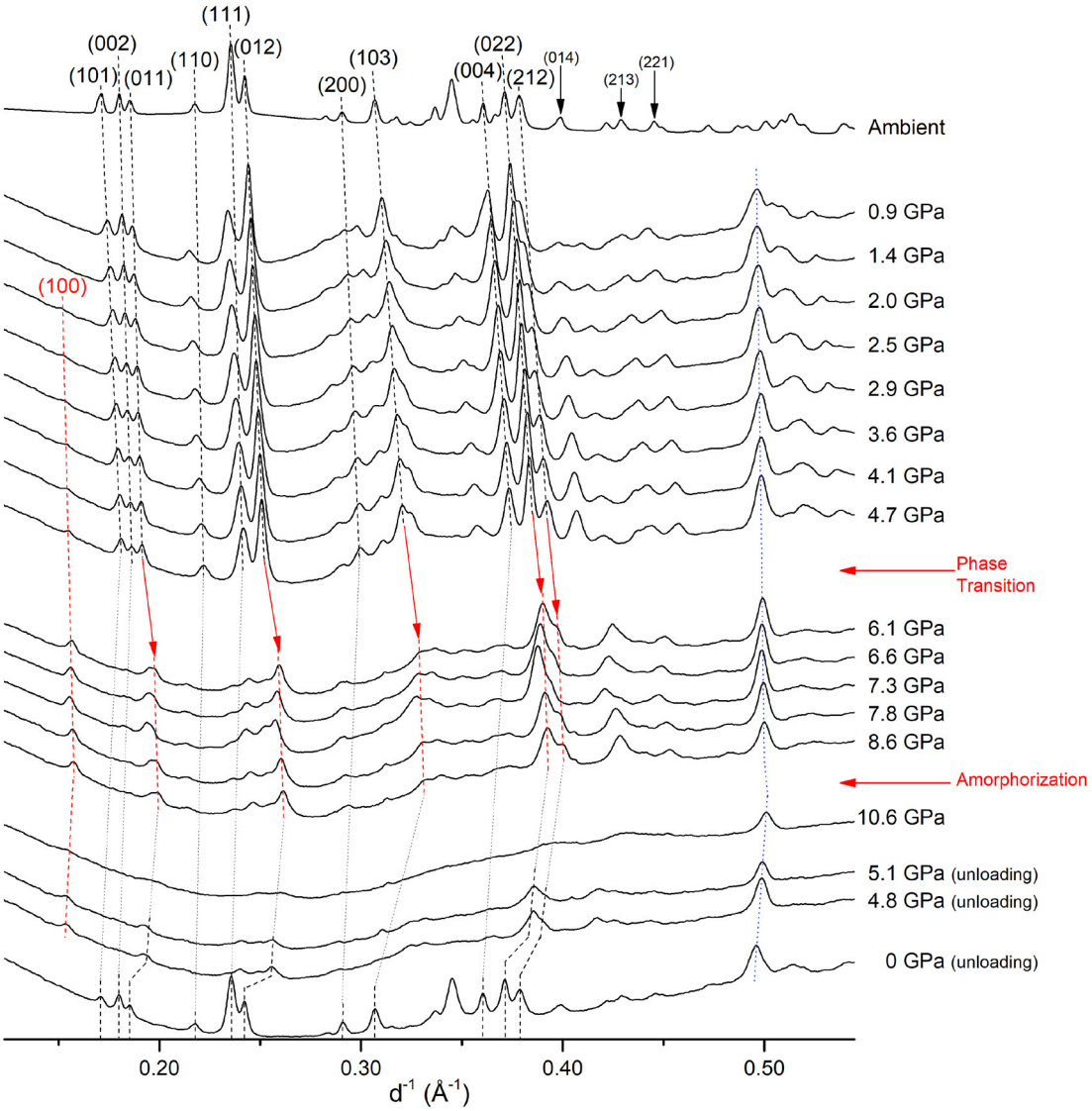

Fig. 2. The diffractograms of struvite-K exposed to different hydrostatic pressures. Grey and red dashed lines indicate the peak shifts of struvite-K. Blue dot line indicates diffraction from the gasket. Other impurity was below the detection limit of XRD through the experiment. Labelled peaks were used for refinement. (For interpretation of the references to colour in this figure legend, the reader is referred to the web version of this article.)

pressure studies [57–60]. At pressure > 2 GPa, a very low-intensity peak (100) at ~1.6 $Å^{-1}$ emerged, indicating a deviation of struvite-K unit cell from $Pmn2_1$ space group.

As hydrostatic pressure reached > 4.7 GPa, the (100) at ~0.16 $Å^{-1}$ appeared as a clear peak, and other existing peaks further broadened. This (100) peak was initially forbidden by the $Pmn2_1$ symmetry at ambient pressure. Its gradual appearance with increasing pressure indicates pressure-induced structural deviation from $Pmn2_1$, and the sudden increase in (100) peak intensity signifies a clear phase transition. While the diffractograms at 4.7 GPa and 6.1 GPa seem apparently different in peak intensity and diffusivity, multiple peaks, e.g., (012), (022), and (212), are traceable across the phase transition, suggesting that the transition is not totally reconstructive. This transition causes a slight displacement of atoms rather than a significantly altered structure, which requires massive disconnection and reconnection of bonds. This pressure-induced phase transition was also observed for cement-based phases (e.g., katoite [55,57] and thaumasite [56]).

As pressure reached 10.6 GPa, struvite-K was fully amorphized, evidenced by the few diffuse scatterings. This stress-induced full amorphization was not observed for many cement-based phases (e.g., calcium (alumino) silicate hydrate, the hydration product of Portland cement) at pressure of ~10 GPa [48,58,61,62]. As the sample was unloaded, the diffraction pattern recovered. The comparable peak positions before loading and after full unloading suggest that the structural deformation was fully reversible.

Table 1 shows the unit cell parameter as a function of applied hydrostatic pressure. Lattice parameters a, b, and c gradually decrease as the applied hydrostatic pressure increases with an exception that a sudden decrease of c was observed when phase transition occurred at 6.1 GPa. When pressure further increased, a, b, and c gradually decreased. After pressure unloaded to 0, the cell parameters recovered. The cell parameters at ambient pressure and fully unloading were highly comparable.

The changes in Biot strain along a-, b-, and c-axis are plotted against applied hydrostatic pressure (Fig. 3A), revealing a phase transition and the anisotropy in the axial stiffnesses. The crystal structure of struvite-K sheds light on the stiffness anisotropy where the b- and c-axis were apparently stiffer than the a-axis before the phase transition. K—O pentahedron and Mg—O octahedron share one edge perpendicular to both b- and c-axis, which can effectively act against distortion in the two directions. K—O pentahedra, being asymmetric, has the shortest bond (2.83 Å) – thus the greatest resistance to deformation – in the bc

Table 1
Pressure–volume data with unit cell parameters for struvite-K as a function of hydrostatic pressure. Pressure error is < 0.15 GPa. The error of lattice parameters is < 0.2%.

	Pressure (GPa)	a (Å)	b (Å)	c (Å)	γ (°)	V (Å^3)
Ambient	0	6.865	6.165	11.098	89.80	469.7
Loading	0.9	6.724	6.130	11.017	87.17	453.1
	1.4	6.653	6.104	10.966	86.67	444.0
	2.0	6.613	6.081	10.915	86.65	437.6
	2.5	6.575	6.056	10.867	86.67	430.6
	2.9	6.544	6.042	10.838	86.62	426.7
	3.6	6.498	6.017	10.787	86.69	420.0
	4.1	6.478	6.000	10.748	86.99	415.9
(Before transition)	4.7	6.448	5.976	10.712	87.20	411.4
(After transition)	6.1	6.447	5.925	10.400	86.19	405.2
	6.6	6.426	5.915	10.346	86.12	401.2
	7.3	6.398	5.886	10.322	86.25	396.6
	7.8	6.380	5.872	10.280	86.52	393.4
	8.6	6.356	5.848	10.244	86.63	389.4
Unloading	0	6.870	6.166	11.096	89.95	470.7

plane, compared to the rest four bonds (2.99–3.13 Å) with components parallel to the a-axis. While P—O tetrahedra and K—O pentahedra share one corner O, which bonds to both P and K in the bc plane, the two polyhedra are only linked by hydrogen bonds along the a-axis. Thus, the crystal maintained the least stiffening mechanisms in a-axis, which explains the anisotropy before phase transition. A molecular dynamics study [43] also suggests that the a-axis is the softest and the stiffness of the b- and c- axes is comparble, and they assigned this anisotropy of strain development to the stability of Mg—O, K—O, and H-bond.

Phase transition (occurring at ~5 GPa, determined from XRD patterns of a repetitive dataset in Appendix A) is unveiled by the discontinuity in the lattice parameters and their respective axial stiffnesses. Note that, in Appendix A, the measured struvite-K crystals were relatively large, resulting in the "anomalous" strong diffractions of a few lattice planes. As the unit cell refinement only requires peak positions as inputs, the peak intensity of the repetitive measurements in Appendix A does not affect any part of the present study. With proper grinding, the diffraction patterns of fine struvite-K crystals in Fig. 2 do not show the "anomalous" strong diffractions from large crystals as in

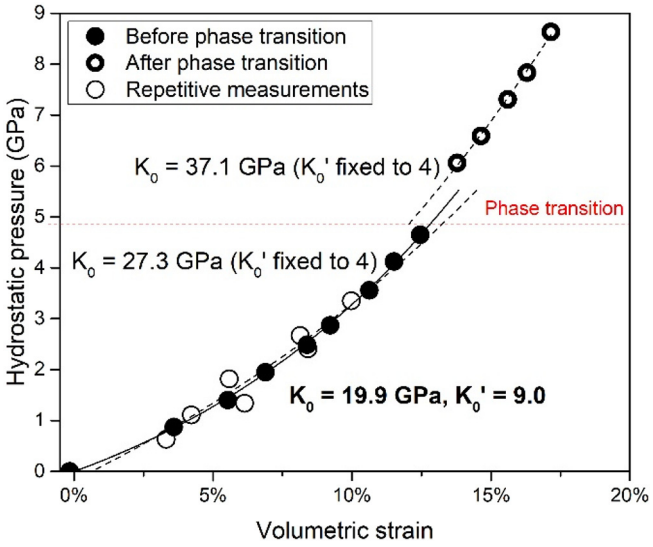

Fig. 4. Hydrostatic pressure as a function of volumetric strain. The dash lines indicate regression curves to the 2nd-order BM-EoS; the solid line indicate regression curve to the 3rd-order BM-EoS. The error in volumetric strain is typically < 1%.

Appendix A. Fig. 3A suggests a high consistency between the repetitive measurements (unfilled symbols) and the original measurements (filled symbol).

Before the phase transition, the incompressibility was lowest along a-axis (Fig. 3A), which experienced stiffening ~1–2 GPa that did not apply to the b- or c-axis. Upon the phase transition, the lattice was most significantly shortened in c-axis while the changes in a- and b-axis were less abrupt. After the phase transition, the incompressibility along a-, b-, and c-axis became comparable ($-1/183$ to $-1/198$ GPa^{-1}), despite the initial anisotropy ($-1/106$ to $-1/150$ GPa^{-1}).

The refined value of γ is 89.95° at ambient pressure (Fig. 3B), conforming to the proposed orthorhombic space group of $Pmn2_1$ for struvite-K. Whereas, γ rapidly dropped to ~87.2° at 0.9 GPa, gradually decreased and stabilized at 86.6–86.7° between 1.4 and 3.6 GPa, and

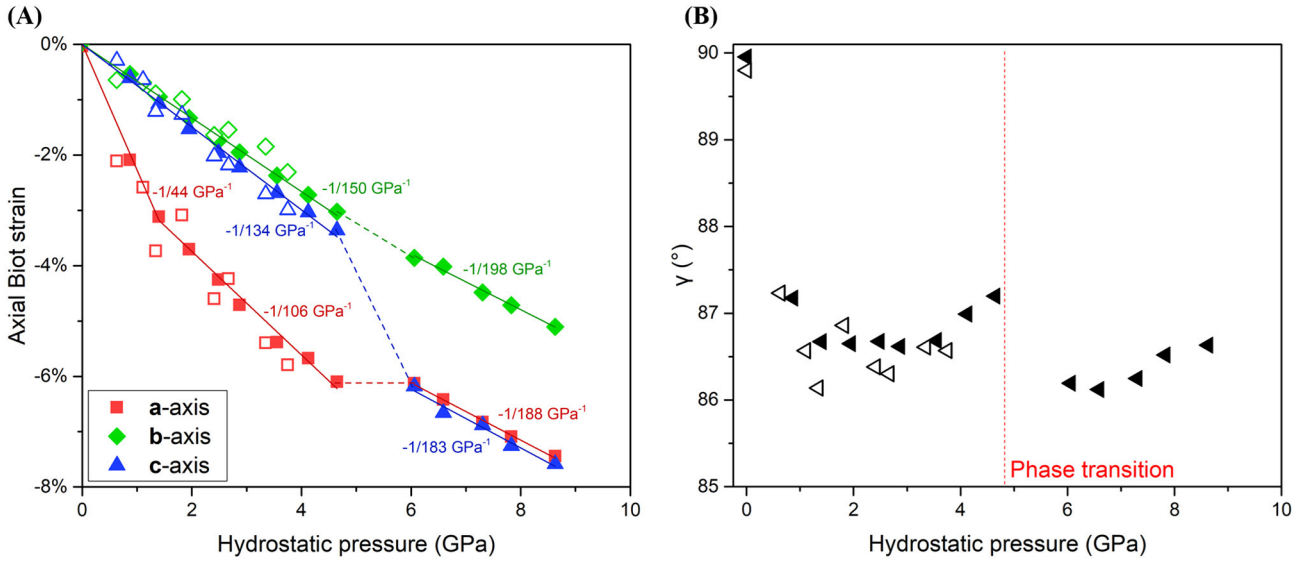

Fig. 3. (A) Axial Biot strain along a-, b-, and c-axis as a function of applied hydrostatic pressure. The filled square, triangle, and diamond represent data collected from one-time continuous measurements; the unfilled symbols represent data from repetitive measurements. The solid lines are best-linearly-fitted lines to the filled symbols, with the indicated slopes; the dash lines across the phase transition are present for eye-guidance. (B) Lattice parameter γ as a function of applied hydrostatic pressure. Filled and unfilled points represent data from one-time continuous measurements and repetitive measurements, respectively. The vertical dash line indicates the approximate pressure of phase transition. The error in axial Biot strain is < 0.7%; the error in hydrostatic pressure is < 0.15 GPa.

Table 2
Fitted parameters of struvite-K.

	K_0 (GPa)	K_0'
Before phase transition		
3rd-order BM-EoS	19.9 ± 3.5	9.0 ± 2.7
2nd-order BM-EoS	27.3 ± 1.1	4 (fixed)
After phase transition		
2nd-order BM-EoS	37.1 ± 1.8	4 (fixed)

then recovered to 87.2° close to the phase transition, at which γ decreased by ~1°, recovering to 86.6° after 8 GPa. Struvite-K developed monoclinic lattice at elevated hydrostatic pressures, as opposed to the orthorhombic lattice at ambient conditions.

The unit cell experienced 17% compressive volumetric strain up to hydrostatic pressure of 8.6 GPa (Fig. 4). The data before and after the phase transition were fitted separately to 2nd- and/or 3rd-order BM-EoS. The bulk modulus before phase transition is fitted with both the filled and unfilled data points (Fig. 4) – i.e., data from multiple measurements – to reduce the statistical errors, especially when the 3rd-orderBM-EoS was applied. The bulk modulus after the phase change was not fitted to the 3rd-order but only the 2nd-order BM-EoS due to limited data points (Table 2). The featureless XRD pattern collected at 10.6 GPa (Fig. 2) suggests that the crystal became X-ray amorphous. Thus, only five measurements were collected in the limited pressure range (~5–10 GPa) for the high-pressure crystalline phase. The crystal gained higher bulk modulus after the phase transition (37.1 GPa compared to 27.3 GPa).

Struvite-K, as the binding phase in MKPC, has comparable density-bulk modulus combination with ettringite and stratlingite, the binding phases in other systems of fast-setting, expansive cement (Fig. 5) while calcium silicate hydrate (C-S-H), the major binding phase of Portland cement, possess ~1.5 times the density and ~3 times the bulk modulus as struvite-K. Periclase, the Mg-bearing raw phase in MKPC, is of both high bulk modulus and high density for the denser atomic packing of this anhydrate. Brucite, sometimes a secondary phase in MKPC originated from excessive Mg content, lies close to the primary hydration

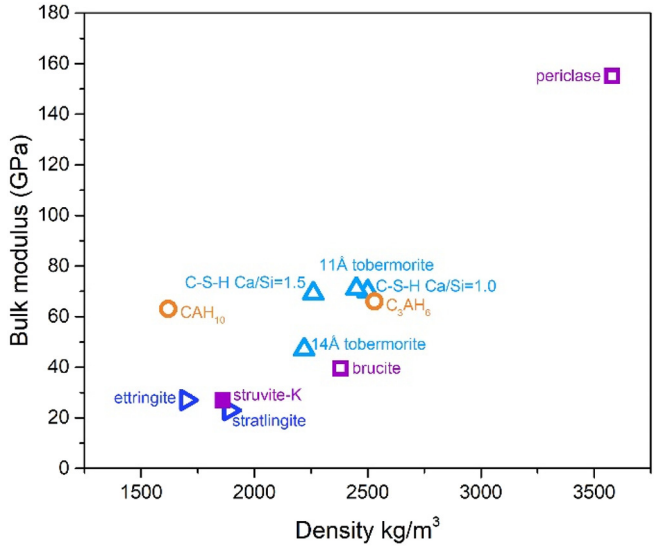

Fig. 5. K_0 of phases related to cement systems as a function of density. C-S-H stands for calcium silicate hydrates, CAH_{10} for $CaO{\cdot}Al_2O_3{\cdot}10H_2O$, and C_3AH_6 (katoite) for $3CaO{\cdot}Al_2O_3{\cdot}6H_2O$. Light blue triangles correspond to Portland cement-based binding phases [48,63–65]; yellow circles correspond to binding phases in calcium-aluminate cement [57]; purple squares correspond to phases in MKPC [66,67]; dark blue triangles correspond to binding phases in multiple cement systems [55,60]. (For interpretation of the references to colour in this figure legend, the reader is referred to the web version of this article.)

products in calcium-aluminate cement and Portland cement in the density-bulk modulus correlation. In general, a strong positive correlation exists between density and bulk modulus of cement-related phases, CAH_{10} being the only outlier. The anomalously high bulk modulus of CAH_{10} for its density is explained that the edge-sharing CaO_8 and AlO_6 polyhedra resists deformation through tilting but allows deformation through the shortening of atomic bonds [57].

The observation of phase transition at ~5 GPa and amorphization at ~10 GPa suggests the inappropriateness of studying the material using nanoindentation. In a nanoindentation study of MKPC [44], the average stress of the indenter very likely reached 8 GPa, and the stress of the indenter tip could approach even higher values, very likely over 10 GPa, due to stress concentration [68]. Note that the elastic modulus of samples obtained from the Basic method used in nanoindentation studies heavily relies on the initial unloading curve [69,70]. This fact implicates that the stress condition of the indenter bypassed the reliable stress range for determining the mechanical properties of struvite-K as the binding phase in MKPC for real applications, where stress rarely exceeds 100 s MPa. Nanoindentation using the Basic method essentially measures the mechanical properties of monoclinic distorted struvite-K, densified phase-changed struvite-K, or even amorphized struvite-K, but it does not measure the original orthorhombic struvite-K. Additionally, as the Poisson's ratio in the nanoindentation study [44] was not given, one can not validate the measured elastic modulus in their study with our measured K_0. Another nanoindentation study of MKPC [40] is not discussed here as the loading/unloading parameters were not given (the maximum stress can not be estimated).

4. Conclusions

The present work studies the mechanical properties of struvite-K, the binding phase in MKPC, at the unit-cell scale using HP-XRD for the first time. This study provides knowledge on the fundamental mechanical properties of struvite-K. The critical findings include:

1. The unit cell transforms from orthorhombic at ambient pressure to monoclinic at hydrostatic pressure < 1GPa. A phase transition occurs at ~5 GPa with an abrupt change in both the unit cell edge length and angle. Further pressurization induces amorphization at ~10 GPa.
2. The unit cell is anisotropic in terms of incompressibility. Before phase transition, the structure is softest in a-axis and comparably stiff in the b- and c-axis; after phase transition, the axial incompressibilities are all enhanced and become isotropic.
3. The bulk modulus of struvite-K is 27 GPa (37 GPa after phase transition), comparable to the binding phases in other cement systems of similar density. The value is an essential input parameter to the multiscale homogenization modelling of the mechanical behavior of MKPC systems.
4. The observed evolution in the struvite-K structure up to 10 GPa suggests an issue with nanoindentation (which applies stress possibly > 10 GPa) to provide reliable information on the mechanical properties of struvite-K under relatively low stress in real structures.

Supplementary data to this article can be found online at https://doi.org/10.1016/j.cemconres.2020.106171.

CRediT authorship contribution statement

Jiaqi Li: Conceptualization, Methodology, Formal analysis, Investigation, Validation, Visualization, Writing - original draft. **Wenxin Zhang:** Formal analysis, Visualization, Writing - review & editing. **Paulo J.M. Monteiro:** Writing - review & editing, Supervision, Funding acquisition.

Declaration of competing interest

The authors declare that they have no known competing financial interests or personal relationships that could have appeared to influence the work reported in this paper.

Acknowledgement

This study is funded by the Republic of Singapore National Research Foundation through a grant to the Berkeley Education Alliance for Research in Singapore (BEARS) for the Singapore-Berkeley Building Efficiency and Sustainability in the Tropics (SinBerBEST) Program. The research conducted at Advanced Light Source is supported by the Director, Office of Science, Office of Basic Energy Sciences, of the U.S. Department of Energy under Contract No. DE-AC02-05CH11231. The authors acknowledge Dr. M. Kunz and Dr. J. Yan for technical assistance at the ALS.

Appendix A. The diffractograms of struvite-K exposed to different hydrostatic pressures from a repetitive series of measurements. Phase transition between 3.8 and 5.0 GPa was observed from the emergence of (100) diffraction peak. The variation in peak intensity from the same (hkl) plane at different pressures is explained by the different preferred orientation of the large struvite-K crystals in regions measured at the different pressures. Only peak positions are need for unit cell refinement. The peak intensity here does not affect any part of the present study

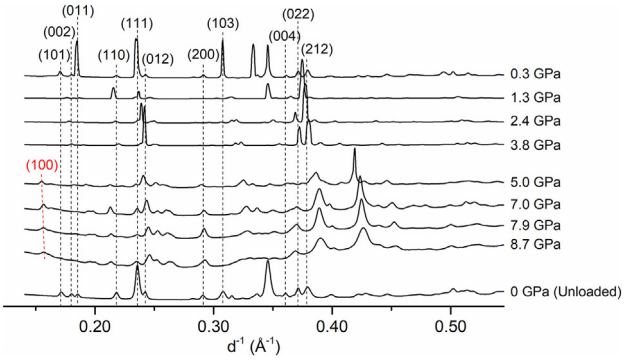

References

[1] A.S. Wagh, S.Y. Jeong, Chemically bonded phosphate ceramics: I, A dissolution model of formation, J. Am. Ceram. Soc. 86 (2003) 1838–1844.
[2] C.K. Chau, F. Qiao, Z.J. Li, Microstructure of magnesium potassium phosphate cement, Constr. Build. Mater. 25 (2011) 2911–2917.
[3] S.A. Walling, J.L. Provis, Magnesia-based cements: a journey of 150 years, and cements for the future? Chem. Rev. 116 (2016) 4170–4204.
[4] L.J. Gardner, S.A. Bernal, S.A. Walling, C.L. Corkhill, J.L. Provis, N.C. Hyatt, Characterisation of magnesium potassium phosphate cements blended with fly ash and ground granulated blast furnace slag, Cem. Concr. Res. 74 (2015) 78–87.
[5] M.A. Haque, B. Chen, Research progresses on magnesium phosphate cement: a review, Constr. Build. Mater. 211 (2019) 885–898.
[6] Z. Ding, B.Q. Dong, F. Xing, N.X. Han, Z.J. Li, Cementing mechanism of potassium phosphate based magnesium phosphate cement, Ceram. Int. 38 (2012) 6281–6288.
[7] K.H. Lee, H.S. Yoon, K.H. Yang, Tests on magnesium potassium phosphate composite mortars with different water-to-binder ratios and molar ratios of magnesium-to phosphate, Constr. Build. Mater. 146 (2017) 303–311.
[8] I. Buj, J. Torras, M. Rovira, J. de Pablo, Leaching behaviour of magnesium phosphate cements containing high quantities of heavy metals, J. Hazard. Mater. 175 (2010) 789–794.
[9] Y. Su, J.M. Yang, D.B. Liu, S.C. Zhen, N.X. Lin, Y.X. Zhou, Effects of municipal solid waste incineration fly ash on solidification/stabilization of Cd and Pb by magnesium potassium phosphate cement, J. Environ. Chem. Eng. 4 (2016) 259–265.
[10] J. Torras, I. Buj, M. Rovira, J. de Pablo, Semi-dynamic leaching tests of nickel containing wastes stabilized/solidified with magnesium potassium phosphate cements, J. Hazard. Mater. 186 (2011) 1954–1960.
[11] L.J. Gardner, V. Lejeune, C.L. Corkhill, S.A. Bernal, J.L. Provis, M.C. Stennett, N.C. Hyatt, Evolution of phase assemblage of blended magnesium potassium phosphate cement binders at 200 degrees and 1000 degrees C, Adv. Appl. Ceram. 114 (2015) 386–392.
[12] J.H. Cho, Y. Eom, T.G. Lee, Stabilization/solidification of mercury-contaminated waste ash using calcium sodium phosphate (CNP) and magnesium potassium, J. Hazard. Mater. 278 (2014) 474–482.
[13] G. Mestres, M.P. Ginebra, Novel magnesium phosphate cements with high early strength and antibacterial properties, Acta Biomater. 7 (2011) 1853–1861.
[14] R.J.Y. Kim, Y.J. Kim, N.S. Choi, I.B. Lee, Polymerization shrinkage, modulus, and shrinkage stress related to tooth-restoration interfacial debonding in bulk-fill composites, J. Dent. 43 (2015) 430–439.
[15] N. Ostrowski, A. Roy, P.N. Kumta, Magnesium phosphate cement systems for hard tissue applications: a review, ACS Biomater. Sci. Eng. 2 (2016) 1067–1083.
[16] Y.W. Weng, S.Q. Ruan, M.Y. Li, L.W. Mo, C. Unluer, M.J. Tan, S.Z. Qian, Feasibility study on sustainable magnesium potassium phosphate cement paste for 3D printing, Constr. Build. Mater. 221 (2019) 595–603.
[17] X. Cao, Z. Li, Factors influencing the mechanical properties of three-dimensional printed products from magnesium potassium phosphate cement material, 3D Concrete Printing Technology, Elsevier, 2019, pp. 211–222.
[18] A. Viani, M. Perez-Estebanez, S. Pollastri, A.F. Gualtieri, In situ synchrotron powder diffraction study of the setting reaction kinetics of magnesium-potassium phosphate cements, Cem. Concr. Res. 79 (2016) 344–352.
[19] B. Lothenbach, B.W. Xu, F. Winnefeld, Thermodynamic data for magnesium (potassium) phosphates, Appl. Geochem. (2019) 111.
[20] H. Ma, B. Xu, Z. Li, Magnesium potassium phosphate cement paste: degree of reaction, porosity and pore structure, Cem. Concr. Res. 65 (2014) 96–104.
[21] H. Lahalle, C.C.D. Coumes, C. Mercier, D. Lambertin, C. Cannes, S. Delpech, S. Gauffinet, Influence of the w/c ratio on the hydration process of a magnesium phosphate cement and on its retardation by boric acid, Cem. Concr. Res. 109 (2018) 159–174.
[22] S. Graeser, W. Postl, H.P. Bojar, P. Berlepsch, T. Armbruster, T. Raber, K. Ettinger, F. Walter, Struvite-(K), KMgPO4·6H(2)O, the potassium equivalent of struvite - a new mineral, Eur. J. Mineral. 20 (2008) 629–633.
[23] X.L. Wang, K.H. Huang, J.B. Gao, X.Z. Shen, C.Y. Lin, G.D. Zhang, Chemical composition and microstructure of uroliths and urinary sediment crystals associated with the feeding of high-level cottonseed meal diet to water buffalo calves, Res. Vet. Sci. 62 (1997) 275–280.
[24] W.D. Sun, J.Y. Wang, K.C. Zhang, X.L. Wang, Study on precipitation of struvite and struvite-K crystal in goats during onset of urolithiasis, Res. Vet. Sci. 88 (2010) 461–466.
[25] B.W. Xu, H.Y. Ma, Z.J. Li, Influence of magnesia-to-phosphate molar ratio on microstructures, mechanical properties and thermal conductivity of magnesium potassium phosphate cement paste with large water-to-solid ratio, Cem. Concr. Res. 68 (2015) 1–9.
[26] Y. Li, Y.Q. Li, T.F. Shi, J.Q. Li, Experimental study on mechanical properties and fracture toughness of magnesium phosphate cement, Constr. Build. Mater. 96 (2015) 346–352.
[27] B.W. Xu, F. Winnefeld, J. Kaufmann, B. Lothenbach, Influence of magnesium-to-phosphate ratio and water-to-cement ratio on hydration and properties of magnesium potassium phosphate cements, Cem. Concr. Res. 123 (2019).
[28] B.W. Xu, B. Lothenbach, H.Y. Ma, Properties of fly ash blended magnesium potassium phosphate mortars: effect of the ratio between fly ash and magnesia, Cem. Concr. Compos. 90 (2018) 169–177.
[29] F. Qiao, C.K. Chau, Z.J. Li, Property evaluation of magnesium phosphate cement mortar as patch repair material, Constr. Build. Mater. 24 (2010) 695–700.
[30] B.W. Xu, B. Lothenbach, F. Winnefeld, Influence of wollastonite on hydration and

properties of magnesium potassium phosphate cements, Cem. Concr. Res. 131 (2020).
[31] H.Y. Ma, B.W. Xu, Potential to design magnesium potassium phosphate cement paste based on an optimal magnesia-to-phosphate ratio, Mater. Des. 118 (2017) 81–88.
[32] L. Yue, C. Bing, Factors that affect the properties of magnesium phosphate cement, Constr. Build. Mater. 47 (2013) 977–983.
[33] A.J. Wang, J. Zhang, J.M. Li, A.B. Ma, L.T. Liu, Effect of liquid-to-solid ratios on the properties of magnesium phosphate chemically bonded ceramics, Mat. Sci. Eng. C Mater. 33 (2013) 2508–2512.
[34] H.Y. Ma, B.W. Xu, J. Liu, H.F. Pei, Z.J. Li, Effects of water content, magnesia-to-phosphate molar ratio and age on pore structure, strength and permeability of magnesium potassium phosphate cement paste, Mater. Des. 64 (2014) 497–502.
[35] A. Viani, K. Sotiriadis, P. Sasek, M.S. Appavou, Evolution of microstructure and performance in magnesium potassium phosphate ceramics: role of sintering temperature of MgO powder, Ceram. Int. 42 (2016) 16310–16316.
[36] L. Yue, S. Jia, C. Bing, Experimental study of magnesia and M/P ratio influencing properties of magnesium phosphate cement, Constr. Build. Mater. 65 (2014) 177–183.
[37] M.R. Ahmad, B. Chen, J. Yu, A comprehensive study of basalt fiber reinforced magnesium phosphate cement incorporating ultrafine fly ash, Compos B Eng. 168 (2019) 204–217.
[38] J. Formosa, A.M. Lacasta, A. Navarro, R. del Valle-Zermeno, M. Niubo, J.R. Rosell, J.M. Chimenos, Magnesium Phosphate Cements formulated with a low-grade MgO by-product: Physico-mechanical and durability aspects, Constr. Build. Mater. 91 (2015) 150–157.
[39] Z. Ding, Z.J. Li, High-early-strength magnesium phosphate cement with fly ash, ACI Mater. J. 102 (2005) 375–381.
[40] Y. Li, G.S. Zhang, Z.G. Wang, Z.Z. Guan, Experimental-computational approach to investigate compressive strength of magnesium phosphate cement with nanoindentation and finite element analysis, Constr. Build. Mater. 190 (2018) 414–426.
[41] Y. Li, G.S. Zhang, Z.G. Wang, Experimental-computational approach to investigate nanoindentation of magnesium potassium phosphate hexahydrate (MKP) with X-CT technique and finite element analysis, Front Mater. 6 (2020).
[42] M. Morales, J. Formosa, E. Xuriguera, M. Niubo, M. Segarra, J.M. Chimenos, Elastic modulus of a chemically bonded phosphate ceramic formulated with low-grade magnesium oxide determined by nanoindentation (vol 41, pg 12137, 2015), Ceram. Int. 42 (2016) 2904–2905.
[43] D.S. Hou, H.D. Yan, J.R. Zhang, P.G. Wang, Z.J. Li, Experimental and computational investigation of magnesium phosphate cement mortar, Constr. Build. Mater. 112 (2016) 331–342.
[44] M. Morales, J. Formosa, E. Xuriguera, M. Niubo, M. Segarra, J.M. Chimenos, Elastic modulus of a chemically bonded phosphate ceramic formulated with low-grade magnesium oxide determined by Nanoindentation, Ceram. Int. 41 (2015) 12137–12146.
[45] M. Morales, E. Xuriguera, J. Formosa, M. Niubo, J.M. Chimenos, M. Segarra, Comment on “Elastic modulus of a chemically bonded phosphate ceramic formulated with low-grade magnesium oxide determined by Nanoindentation”, Ceram. Int. 42 (2016) 3722–3723.
[46] P. Trtik, B. Munch, P. Lura, A critical examination of statistical nanoindentation on model materials and hardened cement pastes based on virtual experiments, Cem. Concr. Compos. 31 (2009) 705–714.
[47] A. Viani, G. Lanzafame, D. Chateigner, Y. El Mendili, K. Sotiriadis, L. Mancini, M. Zucali, B. Ouladdiaf, Microstructural evolution and texture analysis of magnesium phosphate cement, J. Am. Ceram. Soc. 103 (2020) 1414–1424.
[48] G. Geng, R.J. Myers, M.J.A. Qomi, P.J.M. Monteiro, Densification of the interlayer spacing governs the nanomechanical properties of calcium-silicate-hydrate, Sci. Rep. 7 (2017) 10986.
[49] A. Cuesta, P. Rejmak, A. Ayuela, A.G. De la Torre, I. Santacruz, L.F. Carrasco, C. Popescu, M.A.G. Aranda, Experimental and theoretical high pressure study of calcium hydroxyaluminate phases, Cem. Concr. Res. 97 (2017) 1–10.
[50] M.A.G. Aranda, Recent studies of cements and concretes by synchrotron radiation crystallographic and cognate methods (vol 22, pg 150, 2016), Crystallogr. Rev. 22 (2016) 230.
[51] M. Mathew, L.W. Schroeder, Crystal-structure of a struvite analog, Mgkpo4.6h2o, Acta Crystallogr. B 35 (1979) 11–13.
[52] C. Prescher, V.B. Prakapenka, DIOPTAS: a program for reduction of two-dimensional X-ray diffraction data and data exploration, High Pressure Res. 35 (2015) 223–230.
[53] R. Cheary, A. Coelho, Programs XFIT and FOURYA, Deposited in CCP14 Powder Diffraction Library, Engineering and Physical Sciences Research Council, Daresbury Laboratory, Warrington, England, 1996.
[54] J. Laugier, B. Bochu, V. CELREF, Developed at the Laboratoire des Matériaux et du Génie Physique, Ecole Nationale Supérieure de Physique de Grenoble (INPG), 2003.
[55] J.H. Moon, J.E. Oh, M. Balonis, F.P. Glasser, S.M. Clark, P.J.M. Monteiro, Pressure induced reactions amongst calcium aluminate hydrate phases, Cem. Concr. Res. 41 (2011) 571–578.
[56] M. Ardit, G. Cruciani, M. Dondi, G. Garbarino, F. Nestola, Phase transitions during compression of thaumasite, Ca3Si(OH)6(CO3)(SO4)·12H2O: a high-pressure synchrotron powder X-ray diffraction study, Mineral. Mag. 78 (2014) 1193–1208.
[57] G. Geng, J. Li, Y. Zhou, L. Liu, J. Yan, M. Kunz, P.J.M. Monteiro, A high-pressure X-ray diffraction study of the crystalline phases in calcium aluminate cement paste, Cem. Concr. Res. 108 (2018) 38–45.
[58] G. Geng, R.J. Myers, J. Li, R. Maboudian, C. Carraro, D.A. Shapiro, P.J. Monteiro, Aluminum-induced dreierketten chain cross-links increase the mechanical properties of nanocrystalline calcium aluminosilicate hydrate, Sci. Rep. 7 (2017) 44032.
[59] J. Li, W. Zhang, P.J. Monteiro, Synchrotron X-ray Raman scattering shows the changes of the Ca environment in CSH exposed to high pressure, Cem. Concr. Res. 132 (2020) 106066.
[60] S.M. Clark, B. Colas, M. Kunz, S. Speziale, P.J.M. Monteiro, Effect of pressure on the crystal structure of ettringite, Cem. Concr. Res. 38 (2008) 19–26.
[61] J.E. Oh, S.M. Clark, P.J.M. Monteiro, Does the Al substitution in C-S-H(I) change its mechanical property? Cem. Concr. Res. 41 (2011) 102–106.
[62] G. Geng, R.N. Vasin, J. Li, M.J.A. Qomi, J. Yan, H.R. Wenk, P.J.M. Monteiro, Preferred orientation of calcium aluminosilicate hydrate induced by confined compression, Cem. Concr. Res. 113 (2018) 186–196.
[63] J.E. Oh, S.M. Clark, H.R. Wenk, P.J.M. Monteiro, Experimental determination of bulk modulus of 14 angstrom tobermorite using high pressure synchrotron X-ray diffraction, Cem. Concr. Res. 42 (2012) 397–403.
[64] J. Li, W. Zhang, K. Garbev, G. Beuchle, P.J.M. Monteiro, Influences of cross-linking and Al incorporation on the intrinsic mechanical properties of tobermorite, Cem. Concr. Res. 135 (2020) 106170.
[65] J. Li, W. Zhang, P.J.M. Monteiro, The structure and intrinsic mechanical properties of nanocrystalline calcium silicate hydrate, ACS Sustain. Chem. Eng. (2020) (Submitted).
[66] M. Liu, L.-g. Liu, Bulk moduli of wüstite and periclase: a comparative study, Phys. Earth Planet. Inter. 45 (1987) 273–279.
[67] X. Xia, D. Weidner, H. Zhao, Equation of state of brucite; single-crystal Brillouin spectroscopy study and polycrystalline pressure-volume-temperature measurement, Am. Mineral. 83 (1998) 68–74.
[68] H. Bei, E.P. George, J. Hay, G.M. Pharr, Influence of indenter tip geometry on elastic deformation during nanoindentation, Phys. Rev. Lett. 95 (2005) 045501.
[69] G.M. Pharr, A. Bolshakov, Understanding nanoindentation unloading curves, J. Mater. Res. 17 (2002) 2660–2671.
[70] A.C. Fischer-Cripps, A simple phenomenological approach to nanoindentation creep, Mater. Sci. Eng. A 385 (2004) 74–82.